Catalytically Active Bimetallic Nanoparticles Supported on Porous Carbon Capsules Derived From Metal−Organic Framework Composites

Hui Yang,*[†] Siobhan J. Bradley,[‡] Andrew Chan,[§] Geoffrey I. N. Waterhouse,[§] Thomas Nann,[‡] Paul E. Kruger,*[∥] and Shane G. Telfer*[†]

[†]MacDiarmid Institute for Advanced Materials and Nanotechnology, Institute of Fundamental Sciences, Massey University, Palmerston North 4442, New Zealand

[‡]MacDiarmid Institute for Advanced Materials and Nanotechnology, School of Chemical and Physical Sciences, Victoria University of Wellington, Wellington 6140, New Zealand

[§]MacDiarmid Institute for Advanced Materials and Nanotechnology, School of Chemical Sciences, The University of Auckland, Auckland 1142, New Zealand

[∥]MacDiarmid Institute for Advanced Materials and Nanotechnology, Department of Chemistry, University of Canterbury, Christchurch 8140, New Zealand

S *Supporting Information*

ABSTRACT: We report a new methodology for producing monometallic or bimetallic nanoparticles confined within hollow nitrogen-doped porous carbon capsules. The capsules are derived from metal−organic framework (MOF) crystals that are coated with a shell of a secondary material comprising either a metal−tannic acid coordination polymer or a resorcinol−formaldehyde polymer. Platinum nanoparticles are optionally sandwiched between the MOF core and the shell. Pyrolysis of the MOF−shell composites produces hollow capsules of porous nitrogen-doped carbon that bear either monometallic (Pt, Co, and Ni) or alloyed (PtCo and PtNi)

metal nanoparticles. The Co and Ni components of the bimetallic nanoparticles are derived from the shell surrounding the MOF crystals. The hollow capsules prevent sintering and detachment of the nanoparticles, and their porous walls allow for efficient mass transport. Alloyed PtCo nanoparticles embedded in the capsule walls are highly active, selective, and recyclable catalysts for the hydrogenation of nitroarenes to anilines.
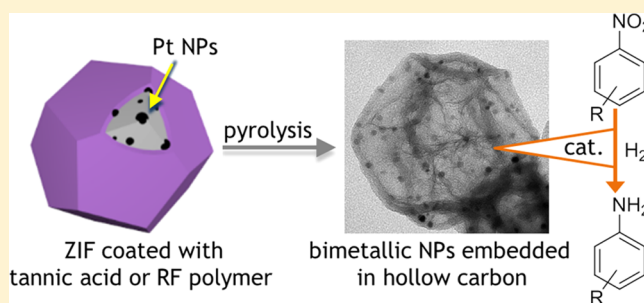
INTRODUCTION

Materials based on nanostructured porous carbon have remarkable properties due to properties such as low density, high surface area, large pore volume, chemical and physical stability, permeability, and electrical conductivity.[1−14] These materials find applications ranging from fuel cells to batteries and supercapacitors. The attractive functional properties of these materials primarily rest on the presence of micropores and/or mesopores. At this nanoscale level the different varieties of porous carbon share many similarities. However, at the mesoscale, their structures are richly varied.[2,15] Among mesoscale structures, discrete, hollow capsules, referred to as hollow porous carbons (HPCs), have garnered considerable attention.[16−26] HPCs can encapsulate, support, and protect secondary materials, such as metal nanoparticles, that are prone to sintering or polymerization. Traditional synthetic methods to HPC composites require a hard template. While this provides fine control over the size of the HPC particles, a significant drawback is that harsh conditions are required for template

removal. For example, HF is commonly used to etch silica templates.[20,22,27,28] To render template removal more facile, soft templates, including organic polymers,[17,25] biological cells,[16] and surfactants,[24] have recently emerged.

Composite materials that bear metal nanoparticles in the interior of porous carbon capsules, abbreviated as NP@HPC, often display excellent catalytic activity.[27−31] Catalyst longevity and recyclability are enhanced by the protective role of the carbon shell. The nanoparticles conventionally comprise just one type of metal; however, bimetallic nanoparticles (BMNPs) such as alloys and core−shell structures can exhibit enhanced catalyst activity, selectivity, and stability compared to monometallic analogues.[32−40] Although a few approaches for the synthesis of MNPs@HPC have been reported,[27,28] synthetic routes to BMNPs@HPC (and indeed BMNPs in general[41]) are still rare.[29,42] This is because the formation of

bimetallic phases often requires a high-temperature reduction reaction, the side-effects of which include phase separation and aggregation. BMNPs can be synthesized at low temperature by employing chemical agents; however, the degree of alloying of the resulting BMNPs is typically low.[43−45]

In light of the attractive properties of BMNPs@HPC, we sought to develop a new strategy for their synthesis that circumvents the aforementioned difficulties. We conceived a synthetic route that employs metal−organic framework (MOF) nanocrystals as sacrificial precursors (Scheme 1). Uniform

Scheme 1. Schematic Illustration of Our Strategy for Using ZIF Nanocrystals as Sacrificial Templates for Carbon Capsules[a]
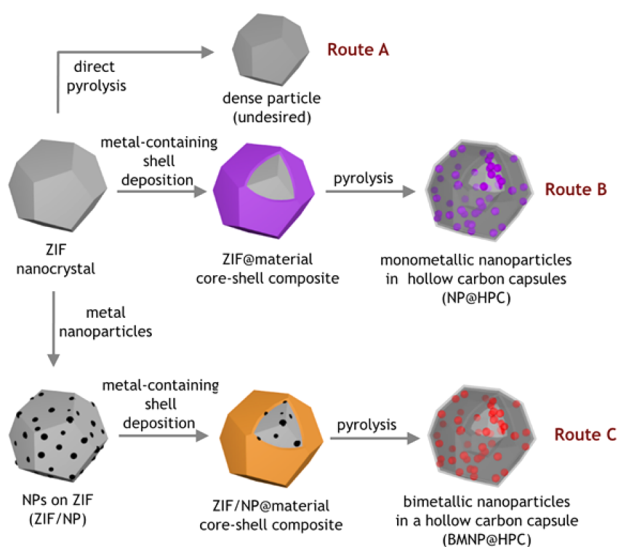
[a]Pre-coating the ZIF crystals with shell composed of a secondary material induces the formation of hollow capsules (*vide infra*) and provides the constituents of embedded metallic nanoparticles.

MOF crystals are used to define the desired shape and dimensions of the final capsules. The surface of the MOF crystals is uniformly coated with a highly cross-linked, metal-containing secondary material that is produced from soluble precursors. The selection of ZIF crystals (ZIF = zeolitic imidazolate framework)[46] as the core of these composites is inspired by observations[47−49] that the deposition of shell layers around ZIF crystals is known to counteract the formation of dense particles that are produced when they are pyrolyzed alone (route A).[50] Here, we take an alternative approach to earlier studies by focusing on metal-containing (rather than organic-only) shell layers.[51] From the plethora of options for this shell layer, we have centered our initial investigations on metal−tannic acid coordination polymers and metal-impregnated resorcinol−formaldehyde polymer. We envisaged that pyrolysis of ZIF@material core−shell composites would produce (i) hollow carbon capsules derived from the organic components of the ZIF and shell and (ii) embedded metal nanoparticles derived from the metallic component of the shell (route B). The carbon produced by ZIF pyrolysis is expected to be both doped with nitrogen[52] and highly porous.[53−56] Access to bimetallic metal nanoparticles supported on the carbon capsules is provided by sandwiching preformed metal nanoparticles between the ZIF and the shell (route C).[57−59] The key attributes of the composite materials that are described herein, i.e., capsule-like morphology, nitrogen doping, and embedded bimetallic nanoparticles, are highly desirable for catalysis.[32−37,60]

■ EXPERIMENTAL SECTION

Full experimental details are included in the Supporting Information.

Synthesis of ZIF@K-TA and Related Composites. In a typical synthesis, 200 mg of ZIF-8 nanocrystals (~200 nm average size) were dispersed in 10 mL of deionized water. Separately, a freshly prepared tannic acid solution (24 mM, 3 mL) was adjusted to pH 8 by the addition of aqueous KOH solution (6 M). Subsequently, the suspension of ZIF-8 nanocrystals was added to the tannic acid solution. After stirring for 5 min, ZIF-8@K-TA was collected by centrifugation, washed several times with deionized water and methanol, and dried overnight under vacuum. Yield: 208 mg. ZIF-8/Pt@K-TA, ZIF-8CoZn@K-TA, ZIF-8CoZn/Pt@K-TA, ZIF-67@K-TA, and ZIF-67/Pt@K-TA composites were synthesized using a similar synthetic route, only changing the ZIF-8 core to ZIF-8/Pt, ZIF-8CoZn, ZIF-8CoZn/Pt, ZIF-67, or ZIF-67/Pt.

Table 1. Summary of the Porous Carbon and Composite Materials Together with Their BET Surface Areas and Pore Volumes

material	precursor	Pt (wt %)[a]	M (wt %)[b]	BET[c]	Pore vol.[d]
NC	ZIF-8	n/a	n/a	1230	0.57
Co/NC	ZIF-8CoZn[e]	n/a	n/d	770	0.50
NHPC_1	ZIF-8@K-TA	n/a	n/a	765	0.71
Co@NHPC_1	ZIF-8@Co-TA	n/a	4.01	520	0.50
Pt@NHPC_1	ZIF-8/Pt@K-TA	1.81	n/a	570	0.81
PtCo@NHPC_1	ZIF-8/Pt@Co-TA	1.72	3.74	390	0.50
Ni@NHPC_1	ZIF-8@Ni-TA	n/a	3.92	440	0.45
PtNi@NHPC_1	ZIF-8/Pt @Ni-TA	1.55	3.5	390	0.51
PtCo/Co@NHPC_1	ZIF-8CoZn/Pt@K-TA	n/d	n/d	n/d	n/d
PtCo/Co@NHPC_2	ZIF-67/Pt@K-TA	n/d	n/d	n/d	n/d
NHPC_2	ZIF-8@RF	n/a	n/a	920	1.27
Pt@NHPC_2	ZIF-8/Pt@RF	1.76	n/a	820	1.05
PtCo@NHPC_2	ZIF-8/Pt@CoRF_a	1.56	1.4	880	0.81
PtCo@NHPC_3	ZIF-8/Pt@CoRF_b	1.63	2.11	800	0.80
PtCo/Co@NHPC_3	ZIF-8/Pt@CoRF_c	n/d	n/d	n/d	n/d

[a]n/a = not applicable; n/d = not determined. [b]M = Co or Ni; metal content determined by AA. [c]BET surface area in m^2/g determined by N$_2$ adsorption at 77 K. [d]Total pore volume in cm^3/g determined by N$_2$ adsorption at 77 K. [e]ZIF-8CoZn is ZIF-8 in which 5% of the metal sites are occupied by cobalt(II) in place of zinc(II).

Synthesis of ZIF@Co-TA and Related Composites. In a typical synthesis, the obtained ZIF-8@K-TA was soaked in a Co(NO$_3$)$_2$·6H$_2$O/methanol (0.02 M, 30 mL) solution. After stirring for 30 min, ZIF-8@Co-TA was collected by centrifugation, washed several times with methanol, and finally dried overnight under vacuum. Yield: 228 mg. ZIF-8/Pt@Co-TA was synthesized using a similar synthetic route but starting from ZIF-8/Pt. ZIF-8@Ni-TA and ZIF-8/Pt@Ni-TA composites were synthesized using a similar synthetic route, only changing the Co(NO$_3$)$_2$·6H$_2$O to Ni(NO$_3$)$_2$·6H$_2$O.

Synthesis of NHPC_1 and Related Composites. ZIF-8@K-TA was transferred into a ceramic crucible and placed in a furnace under a dry argon flow and heated from room temperature to 900 °C over a period of 300 min. After reaching the target temperature, the sample was calcined for a further 3 h at 900 °C then cooled to room temperature to give NHPC_1 (NHPC = nitrogen-doped hollow porous carbon), which was washed with deionized water and methanol, then dried overnight under vacuum. NC-, Co/NC-, and NHPC_1-based composites were prepared in the same way starting from the materials listed in Table 1.

Synthesis of ZIF-8@RF Composites. In a typical synthesis, 15 mg of resorcinol, 3 g of formaldehyde solution (37 wt % in H$_2$O, contains 10−15% methanol as stabilizer), and 15 mg of cetyltrimethylammonium bromide (CTAB) were dissolved in 60 mL of deionized water and stirred at room temperature for 30 min. Subsequently, 200 mg of ZIF-8 nanocrystals were dispersed in this solution by sonication for 10 min. The mixture was then stirred at room temperature for 24 h. ZIF-8@RF was isolated as a pale pink powder by centrifugation and washed several times with deionized water and methanol, then dried overnight under vacuum. Yield: 215 mg. ZIF-8/Pt@RF was synthesized using a similar synthetic route, only changing the ZIF-8 nanocrystals to ZIF-8/Pt. ZIF-8/Pt@RF was subsequently dispersed in 20 mL of aqueous Co(NO$_3$)$_2$·6H$_2$O solution (0.01, 0.02, or 0.03 mol/L) and stirred at room temperature for 30 min before the solid was isolated by centrifugation, washed three times with deionized water, and dried overnight under vacuum. The products are named ZIF-8/Pt@CoRF_a, ZIF-8/Pt@CoRF_b, and ZIF-8/Pt@CoRF_c.

Synthesis of NHPC_2 and Related Composites. ZIF-8@RF was transferred into a ceramic crucible and placed in a furnace under a dry argon flow and heated from room temperature to 900 °C over a period of 300 min. After reaching the target temperature, the sample was calcined for a further 3 h at 900 °C then cooled to room temperature to give NHPC_2. Pt@NHPC_2, PtCo@NHPC_2, and PtCo@NHPC_3 composites were prepared in the same way starting from the materials listed in Table 1.

Hydrogenation of Nitroarenes. In a typical experiment, 0.5 mmol of nitroarenes, 5 mL of methanol, and 20 mg of catalyst were added into an autoclave reactor (50 mL), which was sealed and purged with H$_2$ several times. The vessel was then heated at 50 °C with 6.8 bar H$_2$ under stirring (400 rpm). HPLC analysis used an Econosil silica 10u column and mesitylene as an internal standard.

■ RESULTS AND DISCUSSION

We initially sought to develop route B of Scheme 1: the synthesis of monometallic nanoparticles embedded in hollow porous carbon capsules. ZIF-8 ([Zn(2-methylimidazolate)$_2$]$_n$) nanocrystals were prepared via a facile synthetic route in methanol solution at room temperature.[61] Their size and morphology were examined by scanning electron microscopy (SEM) and transmission electron microscopy (TEM), which revealed them to be polyhedral with edge lengths between 50 and 300 nm (Figure S12). A metal–phenolic coordination polymer, potassium tannic acid (K-TA), was coated as a secondary material onto the ZIF-8 crystal surface to give ZIF-8@K-TA (Figure 1a). This was achieved by briefly exposing the ZIF-8 crystals to an aqueous solution of tannic acid at pH 8. TEM images clearly reveal that the polyhedral shape of the ZIF template is maintained, with the K-TA layer evident as a thin
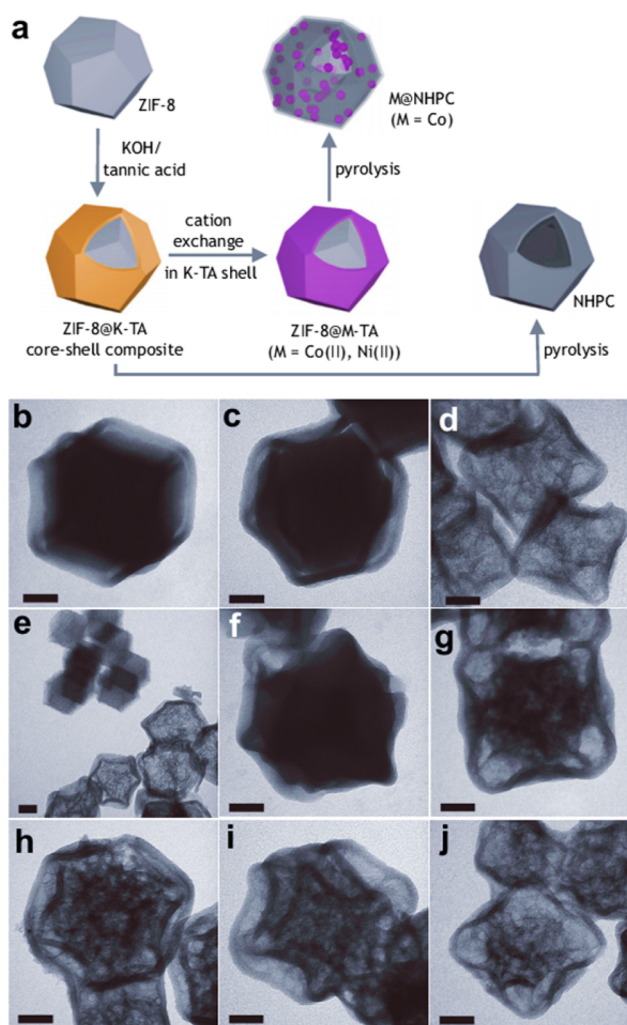

Figure 1. (a) Synthesis of ZIF-8@M-TA core−shell composites and their pyrolysis to produce NHPC_1 and M@NHPC_1 capsules. TEM images of (b) ZIF-8@K-TA, (c) ZIF-8@Co-TA, (d) NHPC_1, (e) NC/NHPC_1 mixture, and (f−j) ZIF-8@K-TA calcined at 500, 600, 700, 800, and 900 °C, respectively. The scale bars represent 50 nm.

(10−15 nm) conformal layer with reduced electron density and a slightly rough exterior (Figure 1b). Powder X-ray diffraction (PXRD) on the ZIF-8@K-TA composite indicates that the crystallinity of the ZIF core is retained (Figure S3). No additional diffraction peaks emanated from the amorphous shell layer. The FTIR spectrum of ZIF-8@K-TA exhibits peaks attributable to both the TA and ZIF-8 components (Figure S49).

Interestingly, postsynthetic cation exchange of the potassium ions in the K-TA shell by cobalt(II) or nickel(II) could be achieved by simply soaking ZIF-8@K-TA in a methanolic solution of Co(NO$_3$)$_2$ or Ni(NO$_3$)$_2$, respectively (Figures 1c, S1, and S3). Replacement of the potassium ions proceeds to completion, as evidenced by EDS (energy-dispersive X-ray spectroscopy). Spectra acquired after cation exchange clearly show the emergence of cobalt/nickel peaks in the new ZIF-8@ M-TA composite together with the complete disappearance of potassium peaks (Figures S14, S16). The shell layer remains conformal with the ZIF-8 template as shown by TEM (Figures 1c and S16). Although metal−tannic acid shells on various other nanomaterials have been reported,[62] to our knowledge this is the first report of ZIF-TA composite materials and the

first demonstration of metal exchange within a tannic acid coordination polymer. The interior of ZIF-8 nanocrystals is known to be strongly hydrophobic; however, their exterior surfaces are hydrophilic due to the existence of terminal N−H functional groups.[63] We postulate that this provides an abundance of H-bonding and coordination sites (in alkaline media) that stimulate the growth of M-TA on the ZIF-8 surface.

We then set about investigating the pyrolysis products of the ZIF/metal−tannic acid core−shell composites. ZIF-8@K-TA was treated at 900 °C under an argon atmosphere (Figure 1a). Remarkably, this transforms the organic components of ZIF-8@K-TA into hollow microcapsules that take on the shape of the ZIF templates (Figure 1d). The capsules obtained in this step are denoted NHPC_1 (NHPC = nitrogen-doped hollow porous carbon, Figure S44). As evidenced by EDS, the capsules are metal-free; the zinc cations of ZIF-8 are reduced to zinc metal, which vaporizes and escapes from the material (Figure S17a,b). Postpyrolysis washing with water and methanol is responsible for removal of the residual potassium salts. X-ray photoelectron spectroscopy (XPS) was used to probe the surface atom composition of the capsules (Figure S44). As expected, the major constituent is carbon, and its 1s binding energies are dominated by graphitic C (284.6 eV) with a minor contribution from C−N carbons (285.6 eV). The existence of nitrogen doping was confirmed by binding energies that can be attributed to pyridine-like (398.3 eV), pyrrole-like (400.8 eV), and nitrogen oxide like (405.8 eV) moieties. NHPC_1 contains 3.8 wt % nitrogen by elemental analysis. Raman spectroscopy indicates that the nitrogen-doped carbon is graphitic and disordered in nature with a G-mode band at 1590 cm^{-1} and a D-mode band at 1350 cm^{-1} (Figure S43).

To assess the mechanism of formation of NHPC_1, we carried out a series of experiments. Particles of nitrogen-doped carbon (NC) were generated by the thermolysis of ZIF-8 nanocrystals (Figure S31a−c,g). The direct comparison of NC and NHPC_1 on the same TEM grid (Figure 1e) highlights the difference in their densities and thus the critical role played by the K-TA shell in inducing the formation of a hollow capsules in the case of NHPC_1. Carbonaceous material of a uniform density was also obtained by pyrolysis of K-TA (Figures S10 and S20). Thermogravimetric analysis of ZIF-8@K-TA under an argon atmosphere established that onset of carbonization of the K-TA layer occurs at 250 °C (Figure S33). Above 550 °C, weight loss due to ZIF-8 decomposition is evident. Large-scale calcination of ZIF-8@K-TA experiments were then carried out at temperature intervals between 500 and 900 °C. The TEM images in Figure 1f−j reveals the evolution of the hollow structures. A core−shell ZIF-8@carbon composite is formed by heating to 500 °C, in which the K-TA layer has carbonized but the ZIF core is unaltered (Figure S7). A calcination temperature of 600 °C induces decomposition of the ZIF-8 core to give ZnO/NC@C and the genesis of capsule formation (Figures 1g and S7). By 700 °C, the density is significantly reduced, indicating that formation of the hollow capsule core is complete. The ZnO peaks disappear from the PXRD pattern at this point due to reduction of ZnO to amorphous Zn metal by carbon (Figures 1h and S7). As the calcination temperature increases to 800 °C then 900 °C, the Zn metal vaporizes and escapes from the material to deliver NHPC_1 (Figure 1d). From the foregoing experiments it is apparent that the ZIF-8 core and the K-TA shell act in concert to produce the hollow carbon capsules. A carbon shell derived from the K-TA layer

forms at ~250 °C. This shell then serves as a substrate on which nitrogen-doped graphitic carbon can nucleate and grow from precursors that are generated by the pyrolysis of ZIF-8 as the as the temperature is raised. Elimination of the zinc occurs by reduction followed by vaporization.

We pursued these pyrolysis experiments to demonstrate that calcination of ZIF-8@Co-TA under argon produces monometallic cobalt nanoparticles supported on porous carbon (Co@NHPC_1, Figure 1a). The CoNPs are found embedded in the NHPC capsule walls (Figure S18a−c,g). The PXRD pattern of Co@NHPC_1 composite (Figure 2a) correlates
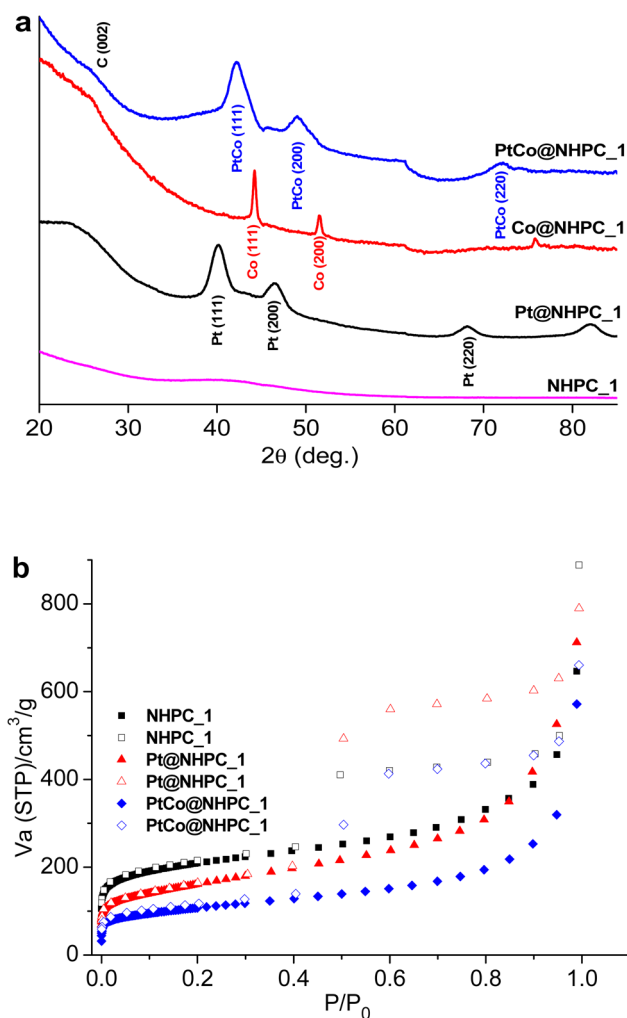

Figure 2. (a) PXRD patterns of NHPC_1 materials; (b) N$_2$ adsorption (filled symbols) and desorption (open symbols) isotherms measured at 77 K for NHPC_1 materials.

with that of *fcc* Co (Powder Diffraction File no. 89−4307, Joint Committee on Powder Diffraction Standards, 2013). No diffraction peaks from CoO or Co$_3$O$_4$ were detected, which indicates that the cobalt exists exclusively in its zerovalent state.

The forgoing results demonstrate that (i) ZIF/metal−tannic acid core−shell composites are excellent precursors to hollow nitrogen-doped carbon microcapsules, and (ii) that the metal ions in the tannic acid layer aggregate into surface-supported nanoparticles in the capsule-forming step. These findings provided a platform for the synthesis of bimetallic nanoparticles embedded in walls of hollow carbon capsules. To tackle the challenge of bimetallic nanoparticles, we decorated the ZIF

crystal surface with platinum nanoparticles (PtNPs) prior to coating with the tannic acid layer (Figure 3a). The second
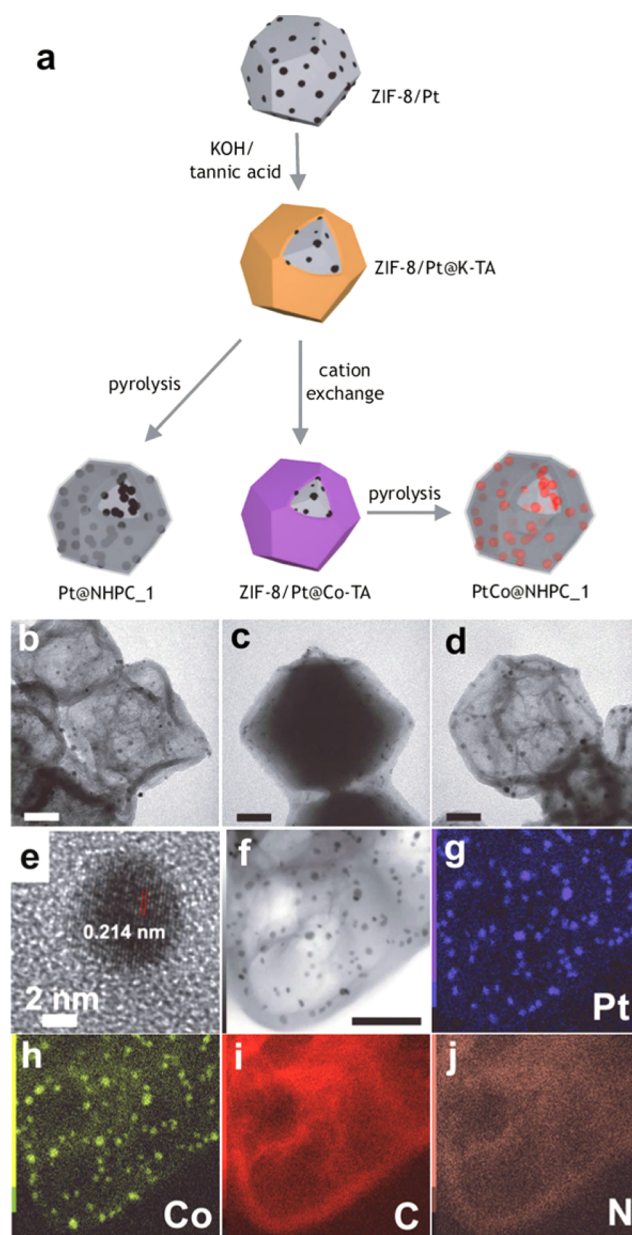

Figure 3. (a) Synthesis of ZIF-8/Pt@M-TA core−shell composites and their pyrolysis to produce NHPC_1, Pt@NHPC_1, and PtCo@NHPC_1 capsules. TEM images of (b) Pt@NHPC_1, (c) ZIF-8/Pt@Co-TA, and (d) PtCo@NHPC_1. (e) HRTEM image showing an individual PtCo bimetallic nanoparticle; (f) STEM image of PtCo@NHPC_1. (j−m) Elemental mapping of PtCo@NHPC_1. The scale bars represent 50 nm, unless otherwise noted.

metal of the bimetallic nanoparticles, cobalt or nickel, is then introduced to the tannic acid shell by cation exchange. During pyrolysis these metal ions can be reduced and migrate to the PtNPs to produce bimetallic alloyed nanoparticles. Furthermore, sandwiching the PtNPs between the core and shell layers is designed to firmly embed the nanoparticles in the walls of the final capsule. This is advantageous for applications in catalysis as it prevents sintering and dissociation of the nanoparticles, but it is difficult to achieve by conventional methods.

We developed an experimental protocol to produce these materials by first decorating the surface of preformed ZIF-8 nanocrystals with 2.8 nm PVP-stabilized PtNPs. TEM on the material obtained by this step, ZIF-8/Pt, verifies that the PtNPs adhere to the exterior ZIF surface (Figure S13a−c,g). A shell of K-TA was then deposited around the Pt/ZIF-8 nanocrystals to produce ZIF-8/Pt@K-TA core−shell particles (Figure 3a). As anticipated, the PtNPs are sandwiched between the ZIF-8 surface and the K-TA layer (Figure S13d−f,h). Replacement of the K^+ by Co^{2+} in the shell of ZIF-8/Pt@K-TA yielded ZIF-8/Pt@Co-TA, in which the outer shell is a cobalt−tannic acid coordination polymer (Figures 3c and S14e,f). The metal exchange step preserves both the particle morphology and crystallinity of the ZIF core (Figures 3c and S4).

ZIF-8/Pt@K-TA and ZIF-8/Pt@Co-TA were then calcined under argon to produce Pt@NHPC_1 and PtCo@NHPC_1, respectively, which feature platinum or platinum/cobalt alloy nanoparticles supported on the walls of NHPC capsules. The TEM images presented in Figure 3b,d confirm the hollow nature of the Pt@NHPC_1 and PtCo@NHPC_1 hosts and the localization of the metal nanoparticles on the capsule walls. No sintering of the nanoparticles into large aggregates was evident, and no nanoparticles were observed on the exterior of the carbon shell. The average diameter of the PtNPs in Pt@NHPC_1 is ∼4.6 nm (Figures 3b and S32), which is 1.8 nm larger than the ZIF-8/Pt@K-TA precursor material. This indicates that some coalescence of the PtNPs occurs during pyrolysis.[64] The average size of the nanoparticles in PtCo@NHPC_1 is ∼5.9 nm (Figures 3d,f and S32), which is consistent with the cobalt atoms from the Co-TA layer fusing with the Pt nanoparticles during pyrolysis to produce alloyed PtCo NPs. This conclusion is supported by a breadth of PXRD, STEM, and XPS data. The PXRD pattern of PtCo@NHPC_1 (Figure 2a) exhibits (111), (200), and (220) reflections at 2θ angles intermediate between those of Pt@NHPC_1 (monometallic PtNPs) and Co@NHPC_1 (monometallic CoNPs). A broad hump from the turbostratic carbon appears around $2\theta = 20°$. HRTEM images of individual PtCoNPs clearly reveal lattice fringes with an interplanar spacing of 2.14 Å corresponding to contrast profiles of the (111) planes (Figure 3e). Scanning transmission electron microscopy (STEM) and the corresponding elemental maps show that the Pt and Co atoms are dispersed uniformly throughout the PtCo nanoparticles (Figure 3f−j). Mapping of the carbon and nitrogen atoms of the capsules confirms their nitrogen-doped carbon character. XPS spectra of PtCo@NHPC_1 demonstrate the presence of platinum, cobalt, carbon, and nitrogen (Figure S46). The Pt (4f) and Co (2p) binding energies align closely with those previously reported for PtCo nanoparticles.[29,65] The nitrogen content is 4.6 wt % as determined by elemental analysis.

Atomic absorption spectroscopy (AA) was employed to determine the metal content of the M@NHPC_1 materials. The Pt content of Pt@NHPC_1 is 1.81 wt %, while the Co content of Co@NHPC_1 is 4.01 wt %. The bimetallic NPs supported on PtCo@NHPC_1 are 1.72 wt % Pt and 3.74 wt % Co. This equates to a Pt/Co ratio of about 1:7.2. The high Co content, previously observed in other PtCoNP materials,[66] and uniform mixing of the two metals is enabled by the similarity of their crystal structures (*fcc* packing) and the melting of the PtNPs during pyrolysis.[64]

The fabrication method presented in Figure 3a can be extended to materials with both monometallic NiNPs and
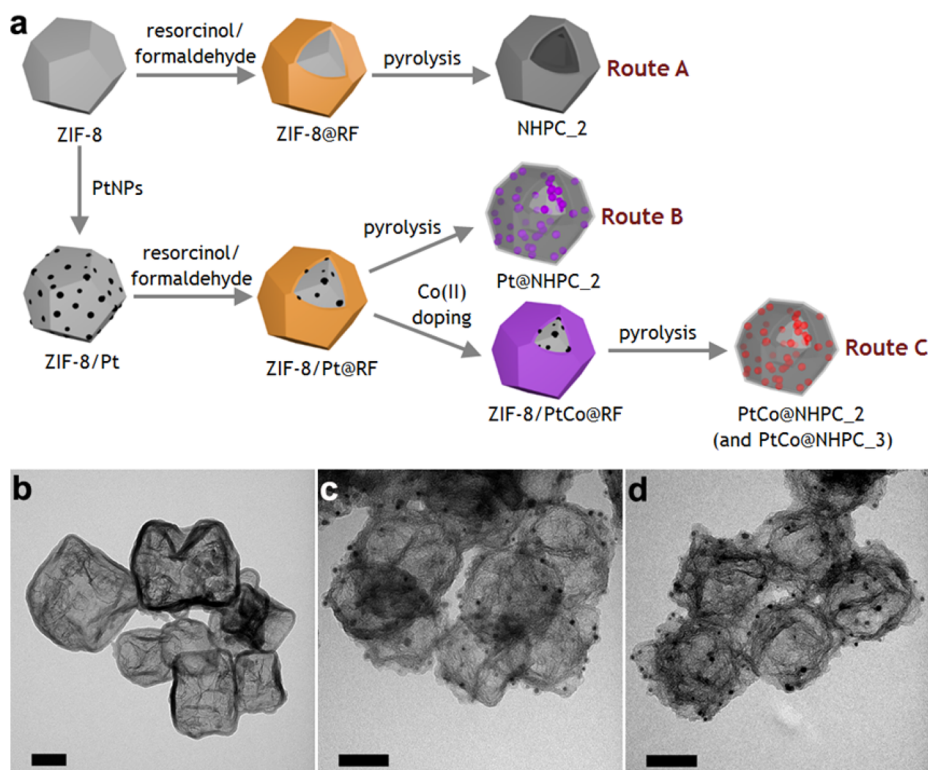
Figure 4. (a) Schematic showing the synthetic routes to NHPC_2 and M@NHPC_2 via the pyrolysis of ZIF-8/RF-polymer core−shell composites. TEM images of (b) NHPC_2, (c) PtCo@NHPC_2, and (d) PtCo@NHPC_3. The scale bars represent 50 nm.

bimetallic NiPtNPs. To illustrate this we fabricated Ni@NHPC_1 (3.92 wt % Ni) and PtNi@NHPC_1 (1.55 wt % Pt, 3.5 wt % Ni) composites. Here, the potassium ions in the TA shell of ZIF-8@K-TA and ZIF-8/Pt@K-TA were replaced by nickel(II) to produce ZIF-8@Ni-TA and ZIF-8/Pt@Ni-TA, respectively (Figure S16). The subsequent pyrolysis of these materials resulted in hollow capsules with metal nanoparticles embedded in their walls (Ni@NHPC_1 and PtNi@NHPC_1, respectively). TEM images resemble the other composites based on NHPC_1 (Figures S18d−f,h and S19). The position of the (111) reflection in the PXRD patterns of Ni@NHPC_1 and PtNi@NHPC_1 is diagnostic of the metal nanoparticle composition and demonstrates that nickel-only nanoparticles are present in Ni@NHPC_1, while alloyed PtNi nanoparticles are present in PtNi@NHPC_1 (Figure S8).

Next, we explored the effect of making modifications to the ZIF core on the formation of the nanoparticle/NHPC composites. When ZIF-8 nanocrystals in which 5% of the zinc(II) ions had been replaced by cobalt(II) were used in place of ZIF-8 nanocrystals, the deposition of the PtNPs and potassium−tannic acid shell proceeded smoothly to produce ZIF-8CoZn/Pt@K-TA (Figures S5, S21, and S22). Upon pyrolysis, metal nanoparticles encapsulated in NHPC shells (PtCo/Co@NHPC_1) were produced (Figure S25a−c,g). We were able to deduce the nanoparticle compositions by PXRD (Figure S9). Both Co and PtCo nanoparticles are present in PtCo/Co@NHPC_1. The Co NPs arise due to the presence of cobalt at the core of the ZIF-8CoZn/Pt@K-TA precursors (rather than being located exclusively in the shell layer as in ZIF-8/Pt@Co-TA). Many of the cobalt atoms fuse to one another, while only a few are able to migrate to the PtNPs to produce PtCo alloy nanoparticles. Another composite with a higher proportion of CoNPs was prepared by employing the

ZIF-67/Pt@K-TA as the sacrificial precursor (ZIF-67 = [Co(2-methylimidizolate)₂]ₙ, Figures S6, S23, and 24). In contrast to PtCo/Co@NHPC_1, large particles and aggregates were observed in PtCo/Co@NHPC_2 (Figures S9 and S25d−f,h) as a consequence of the very high cobalt content of ZIF-67.

By measuring N_2 adsorption isotherms at 77 K, we found all the ZIF/tannic acid composite materials to be porous both before and after thermolysis (Tables 1 and S1). Isotherms of the ZIF@M-TA and ZIF/Pt@M-TA materials typically exhibited high gas uptake and displayed a Type I[67,68] profile. This indicates that the K-TA layer does not block the inherent microporosity of the ZIF core (Figures S34−35). For NHPC_1, M@NHPC, and BMNPs@NHPC materials, the isotherms show typical Type II behavior, indicating the coexistence of a wide range of pore sizes (Figures 2b and S36). Pronounced hysteresis loops became evident during the N_2 desorption phase at pressures between P/P_0 0.95 and 0.4, suggesting the existence of semiclosed ("ink-bottle") pores. The surface areas of these materials were calculated using the BET model and range from 380 to 800 $m^2\ g^{-1}$ (Table 1),[68] while their total pore volume is typically around 0.4−0.8 $cm^3\ g^{-1}$ (Table 1). The pore size distributions calculated using a QSDFT method (Figures S40, S42) reveal a hierarchical pore structure with void spaces in the micro-, meso-, and macropore ranges. It is notable that the carbonaceous material obtained by pyrolysis of K-TA in the absence of a ZIF-8 template lacks porosity (Figure S36 and Table S1). Compared to hollow NHPC_1, ZIF-8-derived NC has a higher gravimetric surface area with no hysteresis and a smaller pore volume (Table 1, Figure S39).

As an alternative to the metal−tannic acid shell, we explored the use of a resorcinol−formaldehyde (RF) polymer as a coating for ZIF-8 (Figure 4a). Copolymerization of resorcinol

and formaldehyde in the presence of ZIF-8 nanocrystals deposits RF polymer as a conformal coating on the ZIF crystal surface (Figures S11 and S26a−c,g) to give ZIF-8@RF. Etching of the ZIF core by dilute aqueous HCl solution produces hollow RF capsules, demonstrating that the RF layer is both thin and contiguous (Figure S27). In addition to providing a substrate for RF deposition, the ZIF-8 nanocrystals also appear to initiate the polymerization reaction so that this occurs exclusively on the crystal surface and not elsewhere in solution owing to its hydrophilic nature and capacity for H-bonding.

Thermolysis of ZIF-8@RF at 900 °C under argon led to volatilization and carbonization of the organic constituents and evaporation of the zinc (Figure 4a, route A). The material produced in this step is denoted NHPC_2. As observed for ZIF-8 coated with tannic acid, the RF polymer coating has an intriguing effect on the thermolysis process. Rather than the dense particles observed in the absence of a shell, NHPC_2 comprises hollow capsules that adopt the size and shape of original composite (Figures 4b and S29a,b). The average capsule wall thickness is around 10 nm. XPS spectra of NHPC_2 (Figure S45) have close parallels with those of NHPC_1, indicating that their surface atomic compositions are similar, i.e., nitrogen-doped carbon.

ZIF-8 nanocrystals decorated with PtNPs could also be coated with a RF shell to give ZIF-8/Pt@RF (Figure 4a, Route B). The PtNPs become sandwiched between the crystal surface and the polymer coating (Figure S26d−f,h). ZIF-8/Pt@RF could be directly converted into a hollow carbonaceous composite, Pt@NHPC_2, by pyrolysis at 900 °C under argon (Figure S30a−c,g). Capsule formation took place without any aggregation of the PtNPs. The Pt loading is 1.76 wt %, as deduced by AA spectroscopy. To make analogs featuring bimetallic nanoparticles, cobalt(II) cations were impregnated into ZIF-8/Pt@RF by soaking in a solution of cobalt nitrate followed by thorough washing with deionized water to produce ZIF-8/Pt@CoRF_a (Figure 4a, route C). The cobalt(II) cations are evident by EDS (Figure S28); however, it is unclear as to whether they are incorporated by displacement of zinc(II) ions from the ZIF core or by coordination to the oxygen donor groups of the RF polymer.

Treatment of ZIF-8/Pt@CoRF_a at 900 °C under argon delivers PtCo@NHPC_2. PXRD and TEM demonstrate that this material comprises alloyed PtCo nanoparticles with fairly uniform diameters (average ∼6 nm) encapsulated within a hollow carbonaceous shell (Figures 4c, 5a, and S32). In the pyrolysis step, the organic components of ZIF-8@CoRF assemble into to NHPC capsules, while the cobalt(II) cations are reduced by carbon and coalesce with PtNPs into embedded PtCo nanoparticles.

The Co/Pt ratio in PtCo@NHPC_2 (1.56 wt % Pt and 1.4 wt % Co) is 2.97:1. This ratio could be altered by simply varying the concentration of cobalt(II) in the soaking step. With a higher concentration, the Co/Pt ratio rose to 4.26:1 in PtCo@NHPC_3 (1.63 wt % Pt and 2.11 wt % Co, Figures 4d and S29e,f). As expected, all four characteristic peaks of the PtCo alloy in the PXRD pattern are shifted toward higher 2θ angles with increasing Co content (Figure 5a). There is a limit to which the cobalt(II) concentration can be beneficially increased in the impregnation step. Monometallic Co nanoparticles are observed in the PXRD pattern of PtCo/Co@NHPC_3 (Figure 5a) due to an overly high cobalt loading in ZIF-8/Pt@CoRF_c. During pyrolysis, a fraction of the Co
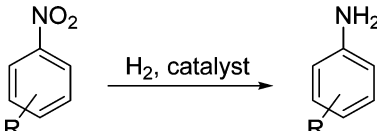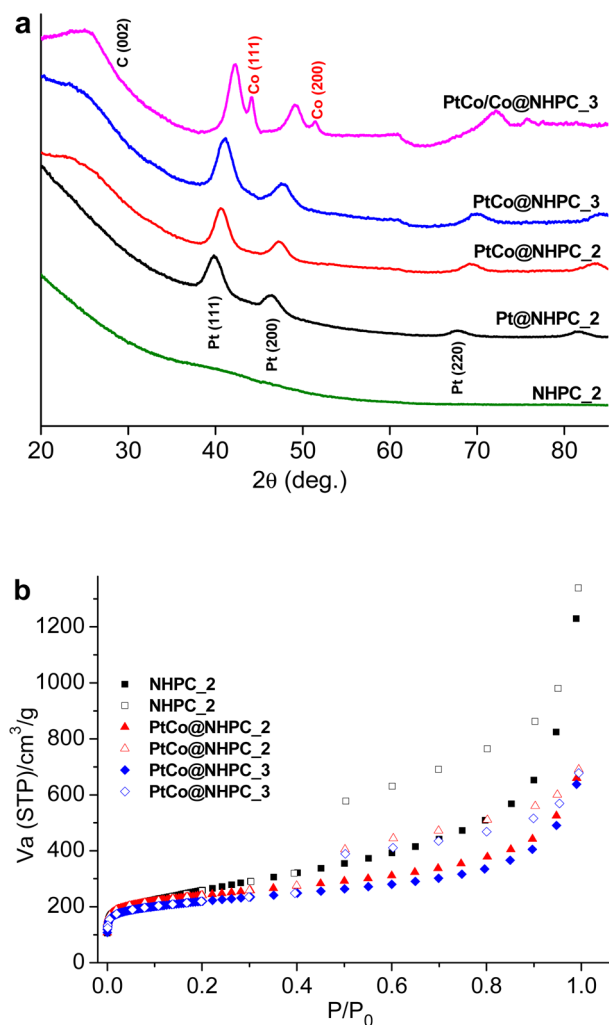

Figure 5. (a) PXRD patterns materials prepared via the thermolysis of ZIF-8-based materials coated with RF polymer; (b) N_2 adsorption (filled symbols) and desorption (open symbols) isotherms measured at 77 K.

atoms ions fuse with PtNPs to form PtCoNPs, while the remainder aggregate to give Co-only NPs (Figures S30d−f,h).

N_2 adsorption measurements at 77 K underscore the high porosity of NHPC_2, Pt@NHPC_2, PtCo@NHPC_2, and PtCo@NHPC_3. The calculated BET surface areas range from 800 to 930 m^2 g^{-1} (Figure 5b and Table 1) with pore volumes from 0.75 to 1.28 cm^3 g^{-1}. Significant hysteresis loops in the isotherm region P/P_0 0.95 to 0.4 indicate ink-bottle pore topologies, and calculated pore size distributions infer that hierarchical pore systems are present (Figure S40).

The selective hydrogenation of nitroarenes to anilines is a challenging and industrially relevant transformation.[69−71] Many Pt-based nanomaterials demonstrate high activity for this reaction.[72−74] High activity often comes at the expense of chemical selectivity, so highly selective catalysts have been the focus of much recent research.[71,74−77] Due to the high cost of noble metal catalysts, Pt-based catalysts are still somewhat limited in practical catalytic applications. One approach to reducing the costs while maintaining activity and selectivity is the implementation of bimetallic catalysts that combine noble metals with inexpensive non-noble metals. In this light, we set about exploring the catalytic properties of the NHPC-supported PtCo nanoparticles described above which have

Table 2. Hydrogenation of Nitroarenes Catalyzed by Metal Nanoparticles Supported on Nitrogen-Doped Hollow Porous Carbon Materials[a]

entry	catalyst	R	conversion (%)	selectivity (%)
1[b]	PtCo@NHPC_1	4-OH	>99.9	98.5
2[c]	Co@NHPC_1		0	
3[c]	Pt@NHPC_1		42.3	98.8
4[c]	NHPC_1		0	
5[b]	PtCo@NHPC_2		>99.9	97.6
6[b]	PtCo@NHPC_3		>99.9	97.2
7[c]	Pt@NHPC_2		42.5	97.0
8[c]	NHPC_1		0	
9[c]	no catalyst		0	
10[b,e]	PtCo@NHPC_1		>99.9	98.7
11[b]	PtCo@NHPC_1	2-Cl	>99.9	99.6
12[b]	PtCo@NHPC_2		>99.9	99.2
13[b]	PtCo@NHPC_3		>99.9	99.7
14[c]	Pt@NHPC_1		67.3	77.0
15[c]	Pt@NHPC_2		65.8	77.2
16[b]	PtCo@NHPC_1	4-COCH$_3$	>99.9	95.2
17[b]	PtCo@NHPC_2		>99.9	96.6
18[b]	PtCo@NHPC_3		>99.9	96.2
19[c]	Pt@NHPC_1		80.5	67.5
20[c]	Pt@NHPC_2		80.6	67.5
21[b]	PtCo@NHPC_1	4-CH$_2$OH	>99.9	99.2
22[b]	PtCo@NHPC_2		>99.9	99.8
23[b]	PtCo@NHPC_3		>99.9	99.1
24[b]	PtCo@NHPC_1	4-OMe	>99.9	99.0
25[b]	PtCo@NHPC_2		>99.9	99.1
26[b]	PtCo@NHPC_3		>99.9	99.1
27[b/d,f]	commercial Pt/C	4-OH	>99.9	low
28[b/d,f]	commercial Pt/C	2-Cl	>99.9	very low

[a]All product distributions determined by HPLC and/or NMR spectroscopy. [b]Standard conditions: 50 °C; 40 min; 20 mg of catalyst; 6.8 bar H$_2$; 0.5 mmol of substrate; methanol as solvent; mesitylene as internal standard. [c]Forcing conditions: 80 °C; 180 min; 50 mg of catalyst; 6.8 bar H$_2$; 0.5 mmol of substrate; methanol as solvent. [d]Scale-up conditions: 80 °C; 180 min; 50 mg of catalyst; 6.8 bar H$_2$; 5 mmol of substrate; methanol as solvent. [e]PtCo@NHPC_1 used as a catalyst after calcination under Ar at 900 °C for 180 min. [f]Overhydrogenation occurs to give saturated products (Figures S60 and 62).

Pt/Co ratios between 1:3 and 1:7. We focused on the hydrogenation of nitroarenes to anilines. To our knowledge, PtCo nanoparticles have not previously been applied as catalysts for this reaction.[29]

In this study, the hydrogenation reactions were typically performed at 50 °C under 6.8 bar of H$_2$ over a period of 40 min (Table 2). A series of control reactions were run to show that the reduction of nitroarenes only takes place in the presence of Pt or PtCo nanoparticles (Table 2, entries 2, 4, 8, and 9).

PtCo@NHPC_1 proved to be a superb catalyst for the hydrogenation of nitroarenes. Employing 4-nitrophenol as substrate, >99.9% of the starting material was consumed to furnish 4-aminophenol with 98.5% selectivity (Table 2, entry 1). PtCo@NHPC_2 and PtCo@NHPC_3 demonstrate similarly impressive levels of activity and selectivity under the same conditions (Table 2, entries 5 and 6). To demonstrate the scalability of the hydrogenation reaction, 5 mmol (0.70 g) of 4-nitrophenol was hydrogenated to produce 4-aminophenol in quantitative yield without any trace of side products (Figure S59). Other nitroarene compounds were also amenable to

hydrogenation by the bimetallic nanoparticle catalysts. For example, 1-chloro-2-nitrobenzene was completely consumed within 40 min to produce 2-chloroaniline with a chemoselectivity in excess of >99% (Table 2, entries 11−13). 4-Nitroacetophenone, 4-nitrobenzyl alcohol, and 4-nitroanisole could also be reduced with high conversion and chemoselectivity, establishing the broad substrate scope of these catalysts. From the literature it is clear that particle composition and size and the nature of the support material are interwoven factors that underlie catalyst performance in this type of system.[39,78,79] We ascribe the high chemoselectivity of these catalysts to the size of the NPs and their interface with the NHPC support, which leads to preferential adsorption of the substrates in an orientation primed for preferential reduction of the nitro group.

The longevity and durability of these three catalysts were established by two tests. First, they were recycled five times and exhibited undiminished activity and selectively (Figure S55). TEM images show that the morphology of the hollow nanostructures is retained and that the PtCoNPs do not

aggregate (Figure S56), and PXRD indicates that the composition of the alloyed PtCoNPs is retained (Figure S57).[80] Second, dry PtCo@NHPC_1 was calcined at 900 °C for 3 h to assess the catalyst stability. TEM images show that the structure of PtCo@NHPC_1 is unaltered (Figures S57 and S58), while its N_2 uptake increases (Figure S58). Most importantly, PtCo@NHPC_1 treated in this way retains its high activity and selectivity for the hydrogenation of 4-nitrophenol (Table 2, entry 10). Turnover frequencies (TOFs) for the hydrogenation of 4-nitrophenol by PtCo@NHPC_1, PtCo@NHPC_2, and PtCo@NHPC_3 were determined to be ∼872, 1136, and 931 $mol_{converted}$ h^{-1} mol_{Pt}^{-1}, respectively.

Pt@NHPC_1 and Pt@NHPC_2 show much lower activity and selectivity than their bimetallic counterparts even under more forcing reaction conditions (Table 2, entries 3, 7, 14, 15, 19, and 20). Furthermore, when commercial Pt on carbon (Pt/C) was used as the catalyst, it showed high activity but very low selectivity. Hydrogenation of the phenyl rings occurs to produce saturated products (Figures S60, S62, and S64).

The foregoing results demonstrate that NHPC-supported PtCoNPs prepared using the strategy outlined in Scheme 1 are exceptional heterogeneous catalysts. The carbon capsules are ideal supports owing to their stability and ability to circumvent aggregation and detachment of the NPs. Their porosity enables the reactants to access the catalytic sites without mass transfer limitations. Alloyed PtCoNPs exhibited higher selectivity and activity than those of the monometallic counterparts,[29,32] and the catalytic activity of the per Pt atom is undiminished even at a Pt/Co ratio of 1:7. These results have positive implications for the development of economical hydrogenation catalysts.

CONCLUSIONS

We have developed a versatile method for the synthesis of nitrogen-doped hollow porous carbon capsules with embedded monometallic or alloyed bimetallic nanoparticles. ZIF-8 nanocrystals decorated with PtNPs then coated with a tannic acid coordination polymer or metal-impregnated RF polymer serve as precursors to these materials. The three components of the precursors play complementary roles in the formation of the NP@NHPC materials. First, the polymer shell on the ZIF-8 nanocrystal surface undergoes thermal decomposition at a relatively low temperature. The carbon formed in this step provides a template for the porous nitrogen-doped graphitic carbon that subsequently emanates from pyrolysis of the ZIF. Hollow capsules are thus produced with a shape and size that is defined by the ZIF crystal. The PtNPs that are enveloped between the ZIF crystal and the shell layer provide a supply of PtNPs, which serve as nucleation points for the supported bimetallic nanoparticles. The second metallic component of the supported nanoparticles is delivered by the shell layer, and the formation of alloyed, rather than segregated, nanoparticles benefits from the spatial proximity of the shell and the PtNPs.

PtCo@NHPC catalyzes the hydrogenation of nitroarenes to anilines with remarkable activity and chemoselectivity. The alloyed nature of the PtCoNPs is crucial to their catalytic performance, and they are robust and recyclable. Furthermore, the hollow capsules prevent sintering and detachment of the nanoparticles, and their porous walls allow for efficient mass transport. These attributes underscore the utility of our synthetic strategy and offer a new avenue to economical hydrogenation catalysts.

The synthetic strategy presented here is straightforward and scalable. We expect that it can be extended to the fabrication of a broad array of other supported multimetallic nanoparticles with predetermined compositions and sizes. Furthermore, it ought to be possible to make heteroatom-doped hollow porous carbon capsules, instead of using nitrogen as in this work. These materials are likely to be valuable catalysts for other chemical and electrochemical processes.

ASSOCIATED CONTENT

ⓈSupporting Information

The Supporting Information is available free of charge on the ACS Publications website at DOI: 10.1021/jacs.6b06736.

> Materials, experimental details, and additional characterization data (^{1}H NMR, atomic absorption spectroscopy, N_2 adsorption/desorption, photographs, powder X-ray diffraction, SEM, TEM, EDS, thermogravimetric analysis, pore size distribution calculations, Raman spectroscopy, XPS, FTIR, HPLC, and turnover frequency calculations) (PDF)

AUTHOR INFORMATION

Corresponding Authors
*E-mail: h.yang2@massey.ac.nz.
*E-mail: paul.kruger@canterbury.ac.nz.
*E-mail: s.telfer@massey.ac.nz. Telephone: (+64) 6 951 7656.

Notes
The authors declare no competing financial interest.

REFERENCES

(1) Meng, Y.; Gu, D.; Zhang, F.; Shi, Y.; Yang, H.; Li, Z.; Yu, C.; Tu, B.; Zhao, D. *Angew. Chem., Int. Ed.* **2005**, *44*, 7053.
(2) Lee, J.; Kim, J.; Hyeon, T. *Adv. Mater.* **2006**, *18*, 2073.
(3) Zhi, L.; Wang, J.; Cui, G.; Kastler, M.; Schmaltz, B.; Kolb, U.; Jonas, U.; Müllen, K. *Adv. Mater.* **2007**, *19*, 1849.
(4) Liang, C.; Li, Z.; Dai, S. *Angew. Chem., Int. Ed.* **2008**, *47*, 3696.
(5) Hu, B.; Wang, K.; Wu, L.; Yu, S. H.; Antonietti, M.; Titirici, M. M. *Adv. Mater.* **2010**, *22*, 813.
(6) Yang, W.; Fellinger, T.-P.; Antonietti, M. *J. Am. Chem. Soc.* **2011**, *133*, 206.
(7) Xu, H.; Guo, J.; Suslick, K. S. *Adv. Mater.* **2012**, *24*, 6028.
(8) Meng, Y.; Voiry, D.; Goswami, A.; Zou, X.; Huang, X.; Chhowalla, M.; Liu, Z.; Asefa, T. *J. Am. Chem. Soc.* **2014**, *136*, 13554.
(9) Yang, S. J.; Antonietti, M.; Fechler, N. *J. Am. Chem. Soc.* **2015**, *137*, 8269.
(10) Zhao, J.; Lai, H.; Lyu, Z.; Jiang, Y.; Xie, K.; Wang, X.; Wu, Q.; Yang, L.; Jin, Z.; Ma, Y.; Liu, J.; Hu, Z. *Adv. Mater.* **2015**, *27*, 3541.
(11) Tang, J.; Liu, J.; Li, C.; Li, Y.; Tade, M. O.; Dai, S.; Yamauchi, Y. *Angew. Chem., Int. Ed.* **2014**, *54*, 588.
(12) Xu, Z.; Zhuang, X.; Yang, C.; Cao, J.; Yao, Z.; Tang, Y.; Jiang, J.; Wu, D.; Feng, X. *Adv. Mater.* **2016**, *28*, 1981.
(13) Xia, Y.; Yang, Z.; Mokaya, R. *Nanoscale* **2010**, *2*, 639.
(14) White, R. J.; Budarin, V.; Luque, R.; Clark, J. H.; Macquarrie, D. J. *Chem. Soc. Rev.* **2009**, *38*, 3401.

(15) Stein, A.; Wang, Z.; Fierke, M. A. *Adv. Mater.* **2009**, *21*, 265.

(16) Ni, D.; Wang, L.; Sun, Y.; Guan, Z.; Yang, S.; Zhou, K. *Angew. Chem., Int. Ed.* **2010**, *49*, 4223.

(17) Lu, A. H.; Li, W. C.; Hao, G. P.; Spliethoff, B.; Bongard, H. J.; Schaack, B. B.; Schuth, F. *Angew. Chem., Int. Ed.* **2010**, *49*, 1615.

(18) Lu, A. H.; Sun, T.; Li, W. C.; Sun, Q.; Han, F.; Liu, D. H.; Guo, Y. *Angew. Chem., Int. Ed.* **2011**, *50*, 11765.

(19) Liu, J.; Yang, T. Y.; Wang, D. W.; Lu, G. Q. M.; Zhao, D. Y.; Qiao, S. Z. *Nat. Commun.* **2013**, *4*, 2798.

(20) Bottger-Hiller, F.; Kempe, P.; Cox, G.; Panchenko, A.; Janssen, N.; Petzold, A.; Thurn-Albrecht, T.; Borchardt, L.; Rose, M.; Kaskel, S.; Georgi, C.; Lang, H.; Spange, S. *Angew. Chem., Int. Ed.* **2013**, *52*, 6088.

(21) Roberts, A. D.; Li, X.; Zhang, H. *Chem. Soc. Rev.* **2014**, *43*, 4341.

(22) Chen, Y.; Xu, P.; Wu, M.; Meng, Q.; Chen, H.; Shu, Z.; Wang, J.; Zhang, L.; Li, Y.; Shi, J. *Adv. Mater.* **2014**, *26*, 4294.

(23) Wang, L.; Sun, Q.; Wang, X.; Wen, T.; Yin, J. J.; Wang, P.; Bai, R.; Zhang, X. Q.; Zhang, L. H.; Lu, A. H.; Chen, C. *J. Am. Chem. Soc.* **2015**, *137*, 1947.

(24) Xu, F.; Tang, Z.; Huang, S.; Chen, L.; Liang, Y.; Mai, W.; Zhong, H.; Fu, R.; Wu, D. *Nat. Commun.* **2015**, *6*, 7221.

(25) Xin, S.; Yin, Y.-X.; Wan, L.-J.; Guo, Y.-G. *Part. Part. Syst. Char.* **2013**, *30*, 321.

(26) Zhang, P.; Qiao, Z.-A.; Dai, S. *Chem. Commun.* **2015**, *51*, 9246.

(27) Ikeda, S.; Ishino, S.; Harada, T.; Okamoto, N.; Sakata, T.; Mori, H.; Kuwabata, S.; Torimoto, T.; Matsumura, M. *Angew. Chem., Int. Ed.* **2006**, *45*, 7063.

(28) Liu, R.; Mahurin, S. M.; Li, C.; Unocic, R. R.; Idrobo, J. C.; Gao, H.; Pennycook, S. J.; Dai, S. *Angew. Chem., Int. Ed.* **2011**, *50*, 6799.

(29) Wang, G. H.; Hilgert, J.; Richter, F. H.; Wang, F.; Bongard, H. J.; Spliethoff, B.; Weidenthaler, C.; Schuth, F. *Nat. Mater.* **2014**, *13*, 293.

(30) Galeano, C.; Baldizzone, C.; Bongard, H.; Spliethoff, B.; Weidenthaler, C.; Meier, J. C.; Mayrhofer, K. J. J.; Schuth, F. *Adv. Funct. Mater.* **2014**, *24*, 220.

(31) Galeano, C.; Meier, J. C.; Soorholtz, M.; Bongard, H.; Baldizzone, C.; Mayrhofer, K. J. J.; Schuth, F. *ACS Catal.* **2014**, *4*, 3856.

(32) Tsang, S. C.; Cailuo, N.; Oduro, W.; Kong, A. T. S.; Clifton, L.; Yu, K. M. K.; Thiebaut, B.; Cookson, J.; Bishop, P. *ACS Nano* **2008**, *2*, 2547.

(33) Wu, Y.; Cai, S.; Wang, D.; He, W.; Li, Y. *J. Am. Chem. Soc.* **2012**, *134*, 8975.

(34) Yu, W.; Porosoff, M. D.; Chen, J. G. *Chem. Rev.* **2012**, *112*, 5780.

(35) Chen, C.; Kang, Y.; Huo, Z.; Zhu, Z.; Huang, W.; Xin, H. L.; Snyder, J. D.; Li, D.; Herron, J. A.; Mavrikakis, M.; Chi, M.; More, K. L.; Li, Y.; Markovic, N. M.; Somorjai, G. A.; Yang, P.; Stamenkovic, V. R. *Science* **2014**, *343*, 1339.

(36) Ge, J.; He, D.; Bai, L.; You, R.; Lu, H.; Lin, Y.; Tan, C.; Kang, Y. B.; Xiao, B.; Wu, Y.; Deng, Z.; Huang, W.; Zhang, H.; Hong, X.; Li, Y. *J. Am. Chem. Soc.* **2015**, *137*, 14566.

(37) Wang, Y.-J.; Zhao, N.; Fang, B.; Li, H.; Bi, X. T.; Wang, H. *Chem. Rev.* **2015**, *115*, 3433.

(38) Singh, A. K.; Xu, Q. *ChemCatChem* **2013**, *5*, 652.

(39) Liu, X.; Wang, D.; Li, Y. *Nano Today* **2012**, *7*, 448.

(40) Sankar, M.; Dimitratos, N.; Miedziak, P. J.; Wells, P. P.; Kiely, C. J.; Hutchings, G. J. *Chem. Soc. Rev.* **2012**, *41*, 8099.

(41) Chen, P.-C.; Liu, X.; Hedrick, J. L.; Xie, Z.; Wang, S.; Lin, Q.-Y.; Hersam, M. C.; Dravid, V. P.; Mirkin, C. A. *Science* **2016**, *352*, 1565.

(42) Galeano, C.; Baldizzone, C.; Bongard, H.; Spliethoff, B.; Weidenthaler, C.; Meier, J. C.; Mayrhofer, K. J. J.; Schüth, F. *Adv. Funct. Mater.* **2014**, *24*, 220.

(43) Zignani, S. C.; Antolini, E.; Gonzalez, E. R. *J. Power Sources* **2008**, *182*, 83.

(44) Bauer, J. C.; Chen, X.; Liu, Q.; Phan, T.-H.; Schaak, R. E. *J. Mater. Chem.* **2008**, *18*, 275.

(45) Cui, X. Z.; Shi, J. L.; Zhang, L. X.; Ruan, M. L.; Gao, J. H. *Carbon* **2009**, *47*, 186.

(46) Banerjee, R.; Phan, A.; Wang, B.; Knobler, C.; Furukawa, H.; O'Keeffe, M.; Yaghi, O. M. *Science* **2008**, *319*, 939.

(47) Yang, S.; Peng, L.; Huang, P.; Wang, X.; Sun, Y.; Cao, C.; Song, W. *Angew. Chem., Int. Ed.* **2016**, *55*, 4016.

(48) Hong, S.; Yoo, J.; Park, N.; Lee, S. M.; Park, J.-G.; Park, J. H.; Son, S. U. *Chem. Commun.* **2015**, *51*, 17724.

(49) Lee, H. J.; Choi, S.; Oh, M. *Chem. Commun.* **2014**, *50*, 4492.

(50) Wang, X.; Zhong, W.; Li, Y. *Catal. Sci. Technol.* **2015**, *5*, 1014.

(51) Yang, H.; Kruger, P. E.; Telfer, S. G. *Inorg. Chem.* **2015**, *54*, 9483.

(52) Aijaz, A.; Fujiwara, N.; Xu, Q. *J. Am. Chem. Soc.* **2014**, *136*, 6790.

(53) Jiang, H. L.; Liu, B.; Lan, Y. Q.; Kuratani, K.; Akita, T.; Shioyama, H.; Zong, F.; Xu, Q. *J. Am. Chem. Soc.* **2011**, *133*, 11854.

(54) Amali, A. J.; Sun, J. K.; Xu, Q. *Chem. Commun.* **2014**, *50*, 1519.

(55) Tang, J.; Salunkhe, R. R.; Liu, J.; Torad, N. L.; Imura, M.; Furukawa, S.; Yamauchi, Y. *J. Am. Chem. Soc.* **2015**, *137*, 1572.

(56) Chen, Y. Z.; Wang, C.; Wu, Z. Y.; Xiong, Y.; Xu, Q.; Yu, S. H.; Jiang, H. L. *Adv. Mater.* **2015**, *27*, 5010.

(57) Lu, G.; Li, S.; Guo, Z.; Farha, O. K.; Hauser, B. G.; Qi, X.; Wang, Y.; Wang, X.; Han, S.; Liu, X.; DuChene, J. S.; Zhang, H.; Zhang, Q.; Chen, X.; Ma, J.; Loo, S. C.; Wei, W. D.; Yang, Y.; Hupp, J. T.; Huo, F. *Nat. Chem.* **2012**, *4*, 310.

(58) Chen, L.; Peng, Y.; Wang, H.; Gu, Z.; Duan, C. *Chem. Commun.* **2014**, *50*, 8651.

(59) Hu, P.; Zhuang, J.; Chou, L. Y.; Lee, H. K.; Ling, X. Y.; Chuang, Y. C.; Tsung, C. K. *J. Am. Chem. Soc.* **2014**, *136*, 10561.

(60) Mistry, H.; Varela, A. S.; Kühl, S.; Strasser, P.; Cuenya, B. R. *Nat. Rev. Mater.* **2016**, *1*, 16009.

(61) Venna, S. R.; Jasinski, J. B.; Carreon, M. A. *J. Am. Chem. Soc.* **2010**, *132*, 18030.

(62) Ejima, H.; Richardson, J. J.; Caruso, F. *Polym. J.* **2014**, *46*, 452.

(63) Zhang, K.; Lively, R. P.; Zhang, C.; Koros, W. J.; Chance, R. R. *J. Phys. Chem. C* **2013**, *117*, 7214.

(64) Nanda, K. K.; Sahu, S. N.; Behera, S. N. *Phys. Rev. A: At., Mol., Opt. Phys.* **2002**, *66*, 013208 DOI: 10.1103/PhysRevA.66.013208.

(65) Li, Z.; Yu, R.; Huang, J.; Shi, Y.; Zhang, D.; Zhong, X.; Wang, D.; Wu, Y.; Li, Y. *Nat. Commun.* **2015**, *6*, 8248.

(66) Han, C.; Lu, Y.; Zhang, J.; Ge, L.; Li, Y.; Chen, C.; Xin, Y.; Wu, L.; Fang, S. *J. Mater. Chem. A* **2015**, *3*, 23274.

(67) Thommes, M.; Kaneko, K.; Neimark, A. V.; Olivier, J. P.; Rodriguez-Reinoso, F.; Rouquerol, J.; Sing, K. S. W. *Pure Appl. Chem.* **2015**, *87*, 1051.

(68) Walton, K. S.; Snurr, R. Q. *J. Am. Chem. Soc.* **2007**, *129*, 8552.

(69) Corma, A.; Serna, P.; Concepcion, P.; Calvino, J. J. *J. Am. Chem. Soc.* **2008**, *130*, 8748.

(70) Wienhöfer, G.; Sorribes, I.; Boddien, A.; Westerhaus, F.; Junge, K.; Junge, H.; Llusar, R.; Beller, M. *J. Am. Chem. Soc.* **2011**, *133*, 12875.

(71) Wei, H.; Liu, X.; Wang, A.; Zhang, L.; Qiao, B.; Yang, X.; Huang, Y.; Miao, S.; Liu, J.; Zhang, T. *Nat. Commun.* **2014**, *5*, 5634.

(72) Kataoka, S.; Takeuchi, Y.; Harada, A.; Takagi, T.; Takenaka, Y.; Fukaya, N.; Yasuda, H.; Ohmori, T.; Endo, A. *Appl. Catal., A* **2012**, *427−428*, 119.

(73) Nie, R. F.; Wang, J. H.; Wang, L. N.; Qin, Y.; Chen, P.; Hou, Z. Y. *Carbon* **2012**, *50*, 586.

(74) Gu, J.; Zhang, Z. Y.; Hu, P.; Ding, L. P.; Xue, N. H.; Peng, L. M.; Guo, X. F.; Lin, M.; Ding, W. P. *ACS Catal.* **2015**, *5*, 6893.

(75) Chen, Y.; Wang, C.; Liu, H.; Qiu, J.; Bao, X. *Chem. Commun.* **2005**, 5298.

(76) Serna, P.; Concepción, P.; Corma, A. *J. Catal.* **2009**, *265*, 19.

(77) Zhang, S.; Chang, C. R.; Huang, Z. Q.; Li, J.; Wu, Z.; Ma, Y.; Zhang, Z.; Wang, Y.; Qu, Y. *J. Am. Chem. Soc.* **2016**, *138*, 2629.

(78) Blaser, H.-U.; Steiner, H.; Studer, M. *ChemCatChem* **2009**, *1*, 210.

(79) Lara, P.; Philippot, K. *Catal. Sci. Technol.* **2014**, *4*, 2445.

(80) The large hysteresis loop observed in the N_2 desorption/desorption isotherm of PtCo@NHPC_1 is retained, while the surface area actually increases from 387 to 591 m^2 g^{-1} (Figure S65). This increase may result from some blocked pores being opened under the reaction conditions.